

BOXY/PEANUT/X-SHAPE BULGES: STEEP INNER ROTATION CURVE LEADS TO BARLENS FACE-ON MORPHOLOGY

H. SALO¹ AND E. LAURIKAINEN¹

Astronomy Research Unit, University of Oulu, FI-90014 Finland

(Dated: Accepted to ApJ, November 8th, 2016)

ABSTRACT

We use stellar dynamical bulge/disk/halo simulations to study whether barlenses (lens-like structures embedded in the narrow bar component) are just the face-on counterparts of Boxy/Peanut/X-shapes (B/P/X) seen in edge-on bars, or if some additional physical parameter affects that morphology. A range of bulge-to-disk mass and size ratios are explored: our nominal parameters ($B/D = 0.08$, $r_{\text{eff}}/h_r = 0.07$, disk comprising 2/3 of total force at $2.2h_r$) correspond to typical MW mass galaxies. In all models a bar with pronounced B/P/X forms in a few Gyrs, visible in edge-on view. However, the pure barlens morphology forms only in models with sufficiently steep inner rotation curves, $dV_{\text{cir}}/dr \gtrsim 5V_{\text{max}}/h_r$, achieved when including a small classical bulge with $B/D \gtrsim 0.02$ and $r_{\text{eff}}/h_r \lesssim 0.1$. For shallower slopes the central structure still resembles a barlens, but shows a clear X-signature even in low inclinations. Similar result holds for bulgeless simulations, where the central slope is modified by changing the halo concentration. The predicted sensitivity on inner rotation curve is consistent with the slopes estimated from gravitational potentials calculated from the $3.6\mu\text{m}$ images, for the observed barlens and X-shape galaxies in the Spitzer Survey of Stellar Structure in Galaxies (S⁴G). For inclinations $< 60^\circ$ the galaxies with barlenses have on average twice steeper inner rotation curves than galaxies with X-shapes: the limiting slope is $\sim 250\text{km/s/kpc}$. Among barred galaxies, those with barlenses have both the strongest bars and the largest relative excess of inner surface density, both in barlens region ($\lesssim 0.5h_r$) and near the center ($\lesssim 0.1h_r$); this provides evidence for bar-driven secular evolution in galaxies.

Keywords: galaxies: bulges — galaxies: evolution — galaxies: kinematics and dynamics — galaxies: structure

1. INTRODUCTION

Majority of strong bars in massive early type disk galaxies exhibit a barlens (bl) morphology: a central lens-like structure embedded in a narrow bar component, identified as a distinct morphological feature in [Laurikainen et al. \(2011\)](#). Recent observational and theoretical studies support the conjecture ([Laurikainen et al. 2007](#)) that such round inner structures are in fact the face-on counterparts of the vertically extended Boxy/Peanut/X-shape (B/P/X) structures commonly seen in barred edge-on galaxies (e.g. [Lütticke, Dettmar & Pohlen 2000](#); [Bureau et al. 2006](#)). Namely, the stellar masses and the axial ratio distributions of their host galaxies are consistent with B/P/X and bl galaxies forming a single population ([Laurikainen et al. 2014](#); [Laurikainen & Salo 2016](#)). Simulation models also show that it is possible to exhibit a B/P/X morphology in edge-on view while the face-on morphology is essentially circular ([Athanassoula et al. 2015](#); [Athanassoula 2016](#)).

Additional support for the B/P/X/bl connection is provided by the very similar colors of the barlens and narrow bar components ([Herrera-Endoqui et al. 2016](#)). This connection of barlenses to vertically extended inner portions of bars indicates that they should not be confused with merger-related classical bulges, or with disky ‘pseudo-bulges’ (*i.e.* inner disks).

The best examples of pronounced barlens morphology in simulations are those of [Athanassoula, Machado & Rodionov \(2013\)](#), which simulations were analyzed in detail in the above mentioned study of [Athanassoula et al. \(2015\)](#). These idealized isolated galaxy N-body + SPH simulations followed the evolution of a stellar+gaseous disk embedded in a tri-axial halo, and included recipes for converting gas into stars. The closest resemblance to observed barlens morphologies was attained with initial gas fractions 20%-80% ([Athanassoula et al. 2015](#)). Recently, barlens morphology was also reported in simulations where disk galaxies were formed

as a result of gas-rich mergers (Athanasoula et al. 2016). However, in most corresponding high-resolution simulations, either with or without gas (e.g. Minchev et al. 2012; Saha et al. 2012; Di Matteo et al. 2013), the formed bars have elongated shapes without round inner barlens components. Also, a close inspection of Athanasoula et al. (2015) models indicates that even there many of the simulated images (see their Fig. 2) contain a slight trace of X-shape morphology in the face-on view. Such X-shape signatures are very rare in the observed nearly face-on barlens galaxies (Laurikainen & Salo 2016), suggesting that the orbital families forming the simulated central structures are not exactly the same as in most observed galaxies.

In this study we perform simple stellar dynamical bulge/disk/halo simulations to address the conditions for obtaining the observed type pure barlens morphology. We vary the parameters influencing the slope of the inner rotation curve, and show how this affects the face-on morphology of the vertically extended inner bar region. The S⁴G survey (Spitzer Survey of Stellar Structure in Galaxies; Sheth et al. 2010) is used as a guide for choosing the simulations parameters, and also as a comparison sample to check the predictions of the simulations.

2. SIMULATIONS

We perform stellar dynamical N-body simulations with GADGET-2 (Springel & Hernquist 2005). The self-consistent initial galaxy models are constructed with the GalactICS software (Kuijken & Dubinski 1995), and they consist of an exponential disk, and a lowered Evans-model (truncated log-potential with a core) for the spherical halo. Compared to the N-body-SPH simulations in Athanasoula, Machado & Rodionov (2013), our simulations contain no gas or star-formation; we also include a small classical bulge (King-model) in the initial conditions, whereas in their study central components could form during the simulation via gas inflow and star formation.

Our nominal model parameters are based on the analysis of the 3.6 μm S⁴G images: to mimic a typical Milky Way (MW) galaxy (with stellar mass $M^* \sim 5 \cdot 10^{10} M_\odot$) we use a bulge-to-disk mass ratio $B/D = 0.08$ and a bulge effective radius $r_{\text{eff}}/h_r = 0.07$, where h_r denotes the scale length of the disk: these were typical bulge values obtained for Hubble types $T = 3$ in the S⁴G pipeline bulge/disk/bar decompositions (Salo et al. 2015). More detailed decomposition, using a separate component for a bar and a barlens (Laurikainen et al. 2014), indicated similar small B/D values even for galaxies with $-2 \leq T \leq 0$. Our halo model is chosen so that at $2.2h_r$ the disk accounts for 65% of the total radial force. This corresponds to the typical value estimated for a MW

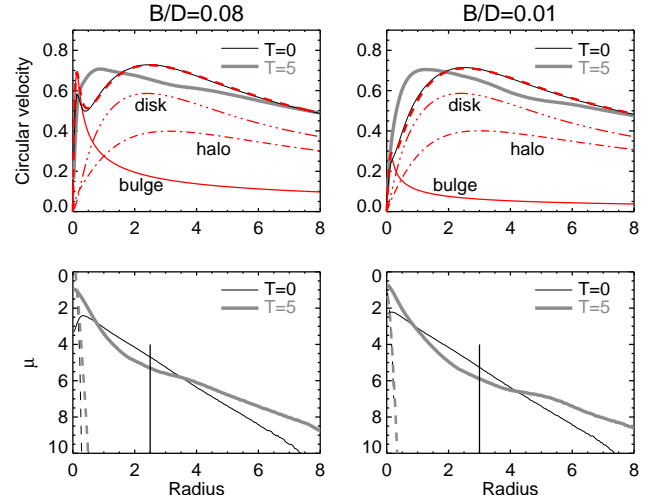


Figure 1. The simulation models. The upper row compares the rotation curves in two simulations with bulge-to-disk mass ratio $B/D = 0.08$ (left) and $B/D = 0.01$ (right). The red curves indicate the initial total rotation curve model from GalactICS, together with separately shown bulge, disk, and halo contributions. The black curves are the actual total circular velocity curve corresponding to the softened forces calculated by GADGET: thin curve refers to initial state and thick curve is after 5 Gyrs. The radius is indicated in units of initial disk scale length; one velocity unit equals ~ 300 km/sec when using the scaling to physical units discussed in the text. The lower frames show the azimuthally averaged surface densities (in magnitude units, with arbitrary zero-point) of the disk (solid lines) and bulge (dashed lines). Again, thin lines refer to the initial model, while thick lines are after 5 Gyrs.

mass galaxy in Díaz-García et al. (2016a), obtained by combining the gravitational field calculated from the 3.6 μm images using the NIRQB-code (Salo et al. 1999; Laurikainen & Salo 2002), with the rotation amplitudes obtained from the HI-kinematics (Courtois et al. 2009). The initial Toomre parameter $Q_T \approx 1.35$ at $2.2h_r$, and the vertical thickness of the disk has a constant scale height $z_0 = 0.2h_r$, which corresponds to ratio of vertical to radial velocity dispersion $\sigma_z/\sigma_r \approx 0.6$ at $2.2h_r$.

The simulation units are fixed by setting the gravitational constant, the mass, and the initial scale length of the disk to unity. To convert to physical units, we identify $m_D = 5 \cdot 10^{10} M_\odot$ and $h_r = 2.5$ kpc, which corresponds to maximum disk contribution to circular velocity ~ 170 km/sec (total circular velocity ~ 215 km/sec; see Fig. 1). Our standard value for gravity softening is $\epsilon = 0.01h_r$, and the time step is $\sim 10^{-2}$ time units; in physical units one time unit corresponds to ~ 10 Myrs. The disk is realized with 10^6 particles, each with mass of $5 \cdot 10^4 M_\odot$. The halo and bulge particles have the same mass as the disk particles.

The rotation curve and the disc & bulge surface density profiles of our nominal simulation model with $B/D = 0.08$ are displayed in Fig. 1, both for the initial

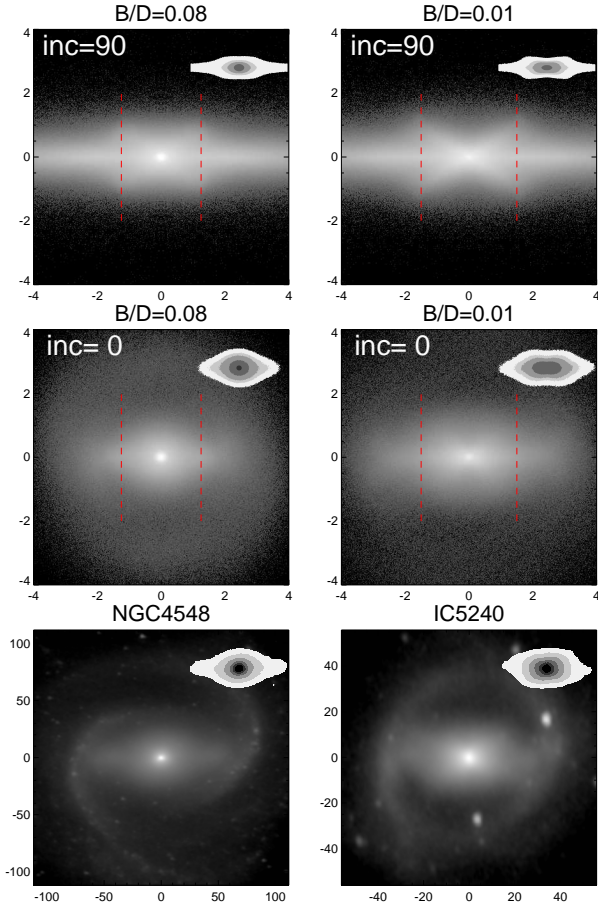


Figure 2. Two simulation models with a small classical bulge: $B/D = 0.08$ (left) and $B/D = 0.01$ (right). Both lead to a B/P/X shape structure when seen edge-on ($i = 90^\circ$, upper row). In face-on view ($i = 0^\circ$, middle) the $B/D = 0.08$ simulation has a morphology very similar to observed barlens galaxies, while the model with $B/D = 0.01$ shows a trace of X-shape signature. The difference is particularly clear in the small insert figures, showing the isophotal contours of the central regions. The lowermost row shows two deprojected images from the S⁴G-survey, NGC 4548 ($i = 39^\circ$, with a barlens), and IC 5240 ($i = 44^\circ$, with an X-shape). In the upper two rows the axis units are in simulation units (initial scale lengths), in the lowermost row in arcseconds.

state and for $T = 5$ Gyrs, after a bar has formed. An otherwise similar model except that $B/D = 0.01$ is also shown. As expected (see e.g. Debattista et al. 2006), the formation of the bar modifies the disk density profile, which becomes more centrally concentrated while the scale length of the outer disk increases. This also modifies the rotation curve, though the central slopes are little affected. In all the following, the discussed rotation curves correspond to those after the bar has already formed.

Figure 2 compares the morphology in simulations with two different bulge-to-disk mass ratios, $B/D = 0.08$

(left) and $B/D = 0.01$ (right). Both simulations form a bar during $T = 1 - 2$ Gyrs, and while the bar starts to form, also the vertical extent of the orbits in the inner part of the bar increases. At $T = 5$ Gyrs (shown in the figure) this has resulted in both cases to a pronounced B/P/X edge-on morphology. The vertical evolution lacks a rapid buckling phase often reported in the literature (Raha et al. 1991), in which sense it is more reminiscent to the resonance heating models (Quillen et al. 2014) where the X is associated to disk stars heated by the 2:1 vertical resonance (Combes et al. 1990; Pfenniger & Friedli 1991; Patsis et al. 2002). Most importantly for the current study, the face-on morphology for $B/D = 0.08$ is very similar to that in massive barred galaxies, with a dominant round barlens structure and a weak thin bar component (compare to NGC 4548 in the lowermost row; see Laurikainen & Salo (2016) for classification of observed barlens categories): this structure survived to the end of the simulation (12 Gyrs). In face-on view the size of the barlens, and that of X-feature in edge-on view, is about 1/2 of bar size, similar to what was found in Athanassoula et al. (2015). In the run with $B/D = 0.01$ the face-on morphology also resembles a barlens, but with a clear waist-like narrowing on the bar minor axis. Most of the simulations in Athanassoula et al. (2015), as well as that in Fig. 1 in Laurikainen et al. (2014) resemble more the simulation with $B/D = 0.01$ than that with $B/D = 0.08$. Although such traces of X-like morphology are not often seen in observed nearly face-on galaxies, one example is IC 5240, with an inclination of $i = 44^\circ$.

The difference in the orbital structure of the two above simulations is illustrated in Fig. 3, showing the time-averaged density distributions of selected disk particle orbits, in a frame co-rotating with the bar. The plots were constructed by sampling the positions of all particles at 500 equally separated instants during the time interval $T = 10 - 11$ Gyrs, when the bar pattern speed Ω_{bar} had attained a constant value (within a few percents). The bar pattern speed was measured by calculating the moment of inertia tensor for all disk particles within 3 distance units from the center, and following the direction of its longest principal axis: the mean rate of change over the time interval was used as Ω_{bar} . The positions of particles were converted to the rotating system and tabulated in two-dimensional bins in xy and xz -planes, where x denotes the coordinate along the bar major axis. The tabulations from all 500 sampling times were added together, yielding the face-on and edge-on projections of the time-averaged density of the selected orbits. We also calculated the Jacobi energies of the particles, $E_j = \frac{1}{2}v^2 + \Phi - \frac{1}{2}\Omega_{bar}^2(x^2 + y^2)$, where Φ is the gravitational potential and v the velocity in the rotating frame: over the sampling interval the E_j of particles

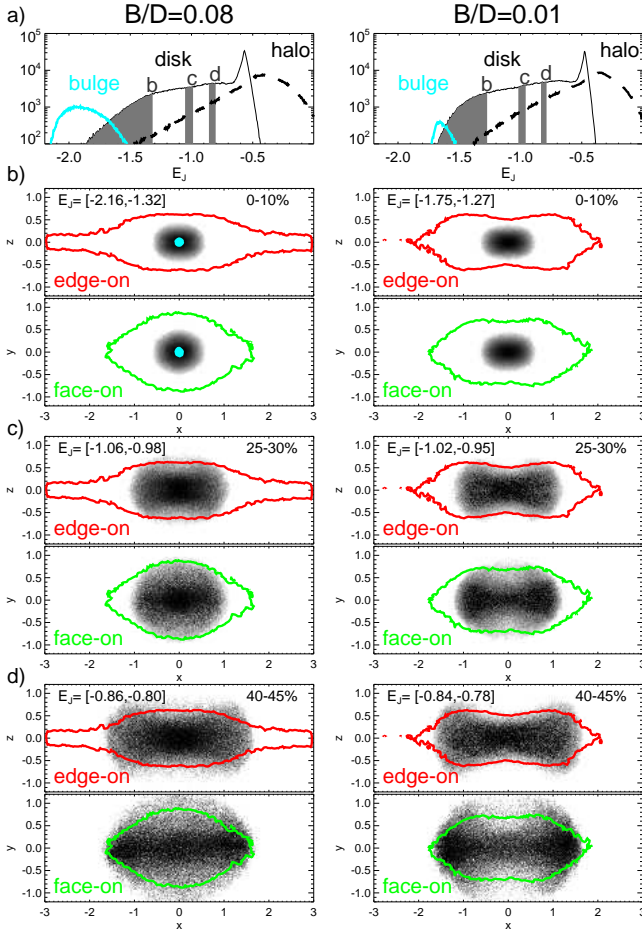


Figure 3. Orbital structure in $B/D = 0.08$ (left column) and $B/D = 0.01$ (right column) simulations. The uppermost row a) shows the distribution of Jacobi energy E_J : the bulge, disk, and halo components are shown separately. The frames b)-d) show the time-averaged (between 10-11 Gyrs) density of orbits, for the disk particles falling in the three E_J ranges indicated by the shaded areas in the histograms of a): the upper frame gives an edge-on view and the lower frame a face-on view. Thick contours outline the edge-on (red) and face-on (green) bar morphology. The blue filled circle in b) indicates where the projected surface density of the classical bulge exceeds that of the disk.

stayed nearly constant.

In Fig. 3, the orbits of disk particles in three different ranges of Jacobi energy are shown separately in frames b), c), and d); the ranges are indicated at the E_J histogram in frame a). In the $B/D = 0.08$ run (left frames), the orbits of the disk particles with E_J in the lowest 10% range (frame b, left) fill a nearly circular region in the face-on projection. For the same E_J range, in the $B/D = 0.01$ run (frame b, right) the density distribution is clearly elongated along the bar major axis. Similar difference concerns the orbits in the energy range 25 – 30% (frame c), which more or less outlines the circular barlens in the $B/D = 0.08$ case, and in the energy range 40 – 45% (frame d), comprising of the orbits with

the largest vertical extent. For the $B/D = 0.01$ model the orbits in frames c) and d) show a clear box-orbit character, with pronounced narrowing in the bar minor axis direction. Clearly, a significant central mass concentration is able to affect the orbital structure in a significant portion of the bar, favoring loop like orbits responsible for the round face-on morphology.

The fundamental difference in the above $B/D = 0.08$ and $B/D = 0.01$ simulations is the much higher central density in the former model, leading to significantly steeper inner rotation curve. The effect of the inner rotation curve is further illustrated in Fig. 4 (uppermost frame), displaying a range of B/D ratios from 0.005 to 0.16, while the bulge effective radius is kept fixed to $r_{\text{eff}} = 0.07h_r$. In these experiments a hint of X-shape face-on morphology (manifests in isophotes as a waist in the minor axis; see the insert figures) appears when the central slope $dV_{\text{cir}}/dr \lesssim 5V_{\text{max}}/h_r$, taking place for $B/D \lesssim 0.02$. The same threshold applies to models where the inner slope is reduced by increasing the bulge effective radius: for example, doubling the effective radius to $r_{\text{eff}} = 0.13h_r$ for $B/D = 0.08$, yields a clear X-signature (middle frame). Similar dependence on rotation curve slope is seen also in models which have no classical bulge component, when the degree of halo central concentration is varied (lowermost frame). Note that the rotation curve is displayed at the time when the bar has formed ($T \sim 5$ Gyrs); the initial h_r is used here mainly to get a rough normalization of the slopes: during the formation of the bar the outer disk scale length typically increases by a factor of 50% – 100%. (see Fig. 1).

Since the simulated morphology is very sensitive to the steepness of the central velocity slope, even the use of too large gravity softening may prevent the pure barlens morphology. This is illustrated in Fig. 5, for the concentrated halo model ('halo3') of Fig. 4, which with our nominal softening ($\epsilon/h_r = 0.01$) leads to barlens morphology. Doubling the softening value ($\epsilon/h_r = 0.02$) leads to clearly elongated central structure. In contrast, reducing ϵ/h_r to 0.005 yields practically similar pure barlens morphology as the nominal value. For our model with $B/D = 0.08$, a similar change of morphology takes place between $\epsilon/h_r = 0.02$ and 0.05. Interestingly, the edge-on morphology is much less affected by increased softening: since the attention in most previous simulations of B/P/X structure has concentrated on the bar vertical structure, the dependence of face-on morphology on softening may have escaped attention.

3. COMPARISON TO OBSERVATIONS

Above simulations suggest that there should be a more or less clear-cut difference (without/with trace of X) in the inner morphology for barlens galaxies with

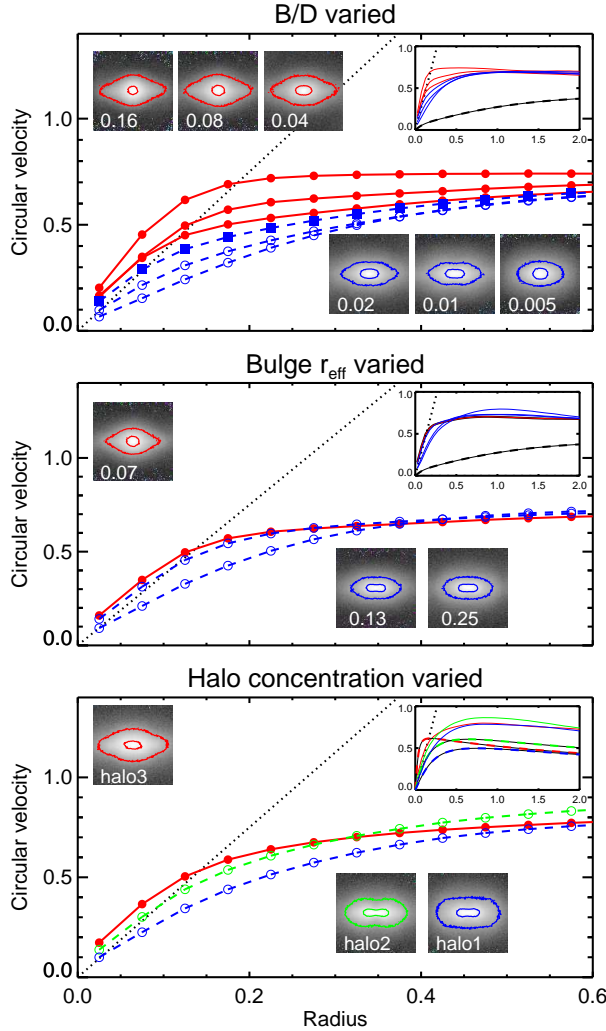


Figure 4. The central slope of circular velocity curve in simulations with different $B/D = 0.005–0.16$ (uppermost frame; r_{eff}/h_r fixed to 0.07) and different bulge $r_{\text{eff}}/h_r = 0.07–0.25$ (middle frame; B/D fixed to 0.08), and in bulgeless simulations with different degree of halo concentration (lowermost frame; halo concentration increases from halo model ‘halo1’ to ‘halo3’); red curves indicate simulations leading to a pure barlens-morphology (round inner morphology with no trace X on face-on view). The dashed line indicates the approximate slope separating the morphologies ($dV_{\text{cir}}/dr = 5V_{\text{max}}/h_r$). The insert figures display the rotation curve on a larger scale, with halo contribution marked with a dashed line; the insert snapshots show the barlens morphology (here using only the disk particles). The rotation curve corresponds to $T=5$ Gyrs; however a practically similar threshold would apply when using the rotation curves from the time before the bar has formed.

steep/shallow inner rotation curve slopes, respectively. Can this be verified with observations? Unfortunately, the number of barlens galaxies with reliably measured rotation curves is very small: for example, the recent study of inner rotation curves based on high resolution H_α kinematics of 29 S⁴G galaxies (Erroz-Ferrer et al. 2016) contains only two galaxies in common

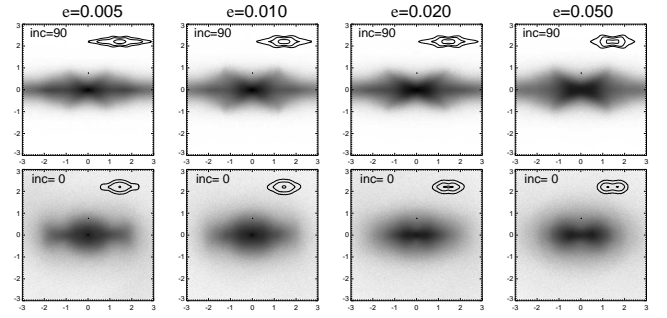


Figure 5. The effect of softening in the simulated inner morphology (total extent of the frames is 6 simulation units). From left to right the softening increases from $\epsilon/h_r = 0.005$ to 0.05. Even a 2-fold softening compared to the nominal value 0.01 destroys the barlens morphology, while with a smaller softening an even slightly better resemblance to observed pure barlens morphology is attained.

with the compilation of barlens & X-shape galaxies in Laurikainen et al. (2014). However, Erroz-Ferrer et al. (2016) also conclude that the inner rotation curves are dominated by baryonic matter (see also Lelli et al. (2013)), based on the comparison of inner slopes of H_α rotation curves with those derived from the S⁴G mass maps (non-stellar contaminants removed based on both $3.6 \mu\text{m}$ and $4.5 \mu\text{m}$ images; Querejeta et al. 2015) using the above mentioned NIRQB code. We may therefore approximate the inner rotation curve slopes with those derived from the mid-IR images: this is done in Fig. 6 for all barlens & X-shape galaxies in S⁴G. Since the rotation curves calculated from the raw $3.6 \mu\text{m}$ S⁴G images and the mass maps differ only very little (Díaz-García et al. 2016a), the slopes in the figure are based on raw $3.6 \mu\text{m}$ images. The median ratio between the observed slopes in Erroz-Ferrer et al. (2016) and our estimated slopes is 0.96 (using the 24 galaxies with observed slopes given in Table 3 of Erroz-Ferrer et al. (2016)).

Figure 6 (upper frame) displays the inner rotation curve slopes (in units of km/sec/kpc) versus galaxy stellar mass. The slopes of barlens galaxies are on average a factor of two steeper than those with X-shape structures. Also, the insert figure indicates that there might be a tendency for a barlens to be rounder when the central slope is steeper, which is in accordance with the simulated behavior. Although the fit is not statistically significant, this dependence on slope is interesting since in Laurikainen et al. (2014) and Athanassoula et al. (2015) no trend was found between the axial ratio of the barlens and the bar strength. Since the visibility of possible weak X-signatures depends strongly on observing direction (Laurikainen & Salo 2016), the lower frame makes a comparison as a function of galaxy inclination. Also, to eliminate the influence of galaxy mass, the slopes are normalized by V_{max}/h_r . Excluding the

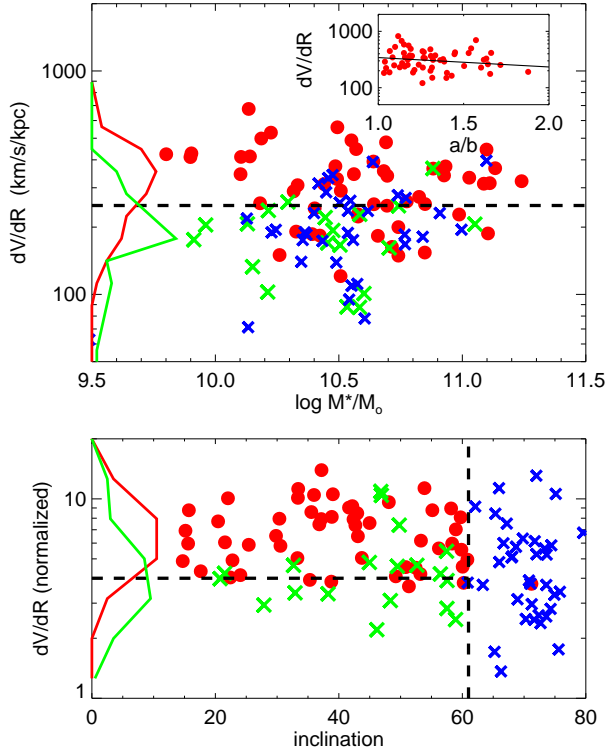


Figure 6. Slopes of the inner rotation curves for S⁴G galaxies, calculated from the 3.6 μ m images. The red circles indicate galaxies with a barlens identification (Laurikainen et al. 2011; Buta et al. 2015), while green ($i < 60^\circ$) and blue crosses ($i > 60^\circ$) stand for galaxies with an X-signature. In the *upper frame* the inner slope is shown versus galaxy stellar mass (M^* from Muñoz-Mateos et al. (2015)), while in the *lower frame* the slope is normalized by V_{max}/h_r and displayed versus galaxy inclination. Here V_{max} is the calculated maximum velocity due to visible mass and h_r is the outer disk scale length from Salo et al. (2015). All parameter values used in Fig. 6 are also listed in Table 1. Histograms in the left show the distributions of barlens and X-shape parent galaxies: they cover all inclinations, so that both prominent edge-on X shapes and weaker X-like signatures at small and intermediate inclinations are included. The insert in the upper frame shows the central velocity slope vs barlens axial ratio (deprojected to the disk plane).

highly inclined galaxies with $i \gtrsim 60^\circ$ (which all are X-shaped), the separation between barlens and X-shape parent galaxies is strikingly clear, in good qualitative agreement with the simulation predictions. In the figure the division between pure barlens and low-inclination X-shape is drawn at 250 km/s/kpc and at $4 V_{max}/h_r$. The latter is close to simulation prediction; note however that here V_{max} refers to stellar-only contribution, and h_r is the observed disc scale length - after the bar has formed.

Three galaxies with X-shaped bars, NGC 4123, NGC 4725 and NGC 7140, appear in the barlens region in Fig. 6, lower frame, where the normalized dV_{cir}/dr is used

(they have $i < 60^\circ$ and $dV_{cir}/dr > 8V_{max}/h_r$; see Table 1). For NGC 4725 this is the case also when expressing the central slope in km/s/kpc (upper frame). In NGC 4725 most probably a large fraction of the central mass concentration inside the X-feature comes from a nuclear bar. In NGC 7140 it is largely due to a nuclear ringlens, and in NGC 4123 due to a point-like nucleus. All these nuclear features are expected to have formed secularly from the disk material. There is no clear indication why these three galaxies deviate from the common trend; this might be related to factors not addressed by the simulations, like the gas content or the halo-to-disk mass ratio.

The morphology of the above simulation models is further studied in Laurikainen & Salo (2016), where we demonstrate that the $B/D = 0.08$ model, when viewed from different inclinations and orientations with respect to the bar major axis, traces well the observed distribution of apparent sizes (normalized to the bar size) and aspect ratios of barlens and X features versus parent galaxy inclination. The same model also reproduces the observed dependence of barlens boxiness parameter on galaxy inclination: for $i \lesssim 40^\circ$ barlenses have $B_4 > 0$, but for larger inclination B_4 gets negative, i.e. isophotes become boxy. This is in line with Erwin & Debattista (2013) who suggested that B/P bulges can be identified at intermediate inclinations ($i = 40 - 60^\circ$) by the boxy inner isophotes of bars.

4. DISCUSSION

The above simulations and comparisons to observations suggest that a steep inner rotation curve slope favors a pure barlens face-on morphology, characterized by a nearly round central appearance. With a shallower rotation curve the orbits in the central regions become more elongated along the bar major axis, leading to an oval shaped bar, or even to an X-shape face-on feature (narrow waist in the minor axis).

The strong constrain on the simulated inner slope is likely to explain why barlenses, which are fairly conspicuous observationally, have not been encountered in simulation studies before Laurikainen et al. (2014) and Athanassoula et al. (2015): typically the classical bulge components employed, if included at all, have been less centrally concentrated than in the current simulations. In Debattista et al. (2004) the problem of not attaining round bar-related bulges in simulations was acknowledged, and it was speculated that extended central objects with $B/D = 0.1 - 0.2$ might be needed, based on Shen and Sellwood (2004) simulations studying the robustness of bars against central black hole masses. In Shen and Sellwood (2004) simulations a rigid halo was assumed, however, very similar conclusions were reached in Athanassoula et al. (2005) using live halos. Our current simulations demonstrate that a

substantially smaller B/D (of a few percents) are sufficient, provided that realistic small effective bulge radii from observations ($r_{\text{eff}}/h_r \lesssim 10\%$) are adopted. Such central mass concentrations are able to affect the orbital morphology up to $\sim 10r_{\text{eff}}$, while still not endangering the survival of the narrow bar. Simulating steep central slopes of course implies a need for small gravity softening: in particular, cosmological simulations so far lack the resolution necessary to resolve the inner bar dynamics (see e.g. the discussion in [Brooks & Christensen 2016](#)).

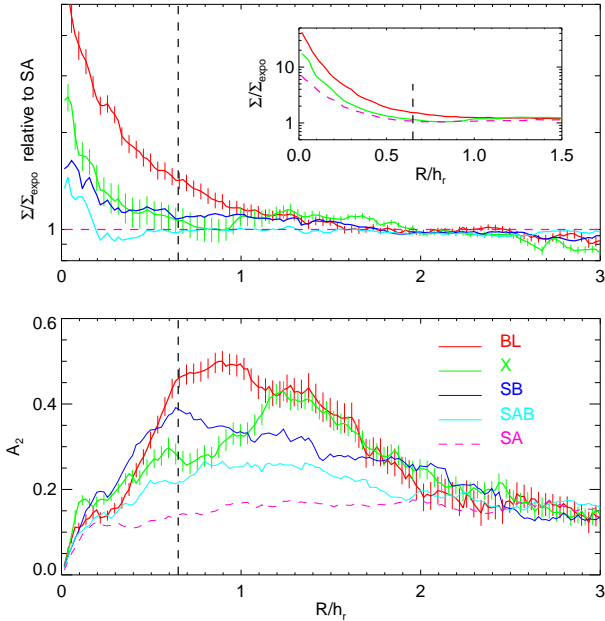


Figure 7. The insert in the *upper frame* shows the median-stacked surface brightness excess of barlens, X-shape, and SA galaxies, relative to their exponential outer disk profiles extrapolated to the center. Decomposition parameters for the disks are from [Salo et al. \(2015\)](#) and the bar family classification from [Buta et al. \(2015\)](#). In the large frame the excess brightness of barlens (bl) and X samples is shown relative to SA galaxies. For comparison also samples of SB and SAB are included (all samples are limited to galaxies with $M^* > 10^{10} M_\odot$, $T \leq 5$). The *lower frame* indicate the medians of A_2 Fourier-amplitude profiles. The vertical dashed line indicates the median barlens size relative to disk scale length ($r/h_r \approx 0.65$; from [Herrera-Endoqui et al. 2015](#)).

We have demonstrated that an inclusion of a small classical bulge in simulations can reproduce the barlens morphology. Does this imply that the observed barlens galaxies harbor classical bulges which were in place already before the bar formed? An alternative is that the central mass concentrations inside the barlens region have formed together with the bar, via bar-induced inflow and star formation. Namely, barlenses are typically associated with strong bars, and to galaxies which have consumed most of their gas. Such inflow was also

the mechanism that created the central mass concentrations in the [Athanasoula et al. \(2015\)](#) simulations, which did not include any initial classical bulge component. Although most of the simulated galaxies had traces of X-shape in their face-on morphology, it is feasible that a somewhat stronger inflow in their models could have created even steeper central rotation slopes and thus more realistic pure barlens morphologies.

Observational evidence for the possible bar-related growth is provided by Fig. 7, which compares the amount of central density excess in barlens galaxies to other types of barred galaxies (with X, and with those SB, SAB galaxies which do not have barlens or X morphology), and to non-barred SA galaxies. Clearly, barlens galaxies have the strongest central excess (consistent with their early T types), both at the region corresponding to the barlens itself, $r/h_r \sim 0.5 - 0.8$, and in the very center, $r/h_r < 0.2$. Among the different galaxy families, the central excess correlates with the strength of the bar (or non-axisymmetric perturbation in general, here measured in terms of A_2 Fourier amplitudes of surface density), supporting the role of bars in building the central concentration. Similar conclusion was recently reached in [Díaz-García et al. \(2016b\)](#) when comparing SB, SAB, and SA galaxies: however the difference is far more pronounced when barlens galaxies are considered.

Nevertheless, the above link between strong bars and central concentrations still leaves open the possibility that the observed central components represent classical bulges which have helped the bars to gain strength, by removing the angular momentum of the bar. Such dependence was seen e.g. in the simulations of ([Athanasoula & Misiriotis 2002](#)), where the bar A_2 maximum was nearly doubled in a model that included a classical bulge component, compared to a model with only disk and halo components. However, the classical bulge in those simulation was quite extended and massive, with $B/D = 0.60$. In the current simulations with small compact classical bulges the strength of the bar is practically independent of the adopted initial B/D , so that no similar straight-forward connection can be made. Clearly, spectroscopic observations of the stellar ages and metallicities would be needed to distinguish between the diskly pseudo-bulge/classical bulge character of the central concentrations in barlens galaxies.

5. CONCLUSIONS

The barlens-sized central light concentrations in early-type disk galaxies are often identified as massive classical bulges. In this paper we have provided further evidence that, at least in the case of barred galaxies, they represent B/P/X/bl structures related to secular evolution of bars. However, the exact morphology at low galaxy inclination depends on the galaxy mass distribution.

Our main conclusions are the following:

1) Stellar dynamical simulations, using parameter values appropriate for MW mass galaxies, indicate that a steeply rising inner rotation curve is required for obtaining a pure barlens morphology (no trace of X in low inclination view). In the current simulations this was achieved by including a small classical bulge to the initial values, or by using a sufficiently centrally concentrated halo. The threshold inner slope in simulations is $dV_{cir}/dr \sim 5V_{max}/h_r$.

2) The simulated behavior is in qualitative agreement with slopes derived from S^4G 3.6 μm images, which indicate that barlens galaxies have steeper baryonic rotation curves ($dV_{cir}/dr \gtrsim 250$ km/sec/kpc) than the galaxies which exhibit X-signature even at $i < 60^\circ$.

3) Comparisons of stacked surface density profiles indicate that barlens galaxies have larger A_2 amplitudes than any other type of barred galaxies. They also have the largest relative excess of inner surface density (within $r/h_r < 0.2$), which can be interpreted as evidence for bar induced inflow in the past.

6. ACKNOWLEDGMENTS

We thank the referee for useful suggestions on how to clarify the presentation of the results. This work was supported by the *DAGAL* network: People Programme (Marie Curie Actions) of the European Unions Seventh Framework Programme FP7/2007-2013 under REA grant agreement number PITN-GA-2011-289313. The grant from Academy of Finland (n:o 297738) is also acknowledged.

REFERENCES

- Athanassoula, E., & Misiriotis, A. 2002, MNRAS, 330, 35
- Athanassoula, E., Lambert, J. C., Dehnen, W. 2005, MNRAS, 363, 496
- Athanassoula, E., Machado, R. E. G., Rodionov, S. A. 2013, MNRAS, 429, 1949
- Athanassoula, E., Laurikainen, E., Salo, H., Bosma, A. 2015 MNRAS 454, 3845
- Athanassoula, E. 2016, in Galactic Bulges (Eds. Laurikainen, E., Peletier, R., Gadotti, D), Astrophysics and Space Science Library, Volume 418. Springer International Publishing Switzerland, 2016, p. 391
- Athanassoula, E., Rodionov, S. A., Peschken, N., Lambert, J. C. 2016 ApJ 821, 90
- Brooks A., Christensen C. 2016, in Galactic Bulges (Eds. Laurikainen, E., Peletier, R., Gadotti, D), Astrophysics and Space Science Library, Volume 418. Springer International Publishing Switzerland, 2016, p. 317
- Bureau M., Aronica G., Athanassoula E., et al. 2006, MNRAS, 370, 753
- Buta, R et al. 2015 ApJS217, 32
- Combes F., Debbasch F., Friedli D., Pfenniger D. 1990, AA, 233, 81
- Courtois, H. M. and Tully, R. B. and Fisher, J. R et al. 2009 AJ138, 1938
- Debattista, V.P., Carollo, C.M., Mayer, L., Moore, B. 2004, ApJ 604, L96
- Debattista, V. P., Mayer, L., Carollo, C. M., et al. 2006, ApJ, 645, 209
- Díaz-García, S, Salo, H., Laurikainen, E, Herrera-Endoqui, M 2016 AA 7, A160
- Díaz-García, S, Salo, H., Laurikainen, accepted to AA (arXiv:1607.07317)
- Di Matteo, P., Haywood, M., Combes, F., Semelin, B., Snaith, O. N. 2013 AA 553, A102
- Erroz-Ferrer, S. and Knapen, J. H. and Leaman, R. and Díaz-García et al. 2016 MNRAS 458, 1199
- Erwin P., Debattista V. 2013, MNRAS, 431, 3060
- Herrera-Endoqui, M., Díaz-García, S., Laurikainen, E., Salo, H. 2015, A&A, 582, A86
- Herrera-Endoqui, M, Salo, H., Laurikainen, E, Knapen, J., accepted to AA (arXiv:1610.02330)
- Kuijken, K. and Dubinski, J. 1995 MNRAS 277, 1341
- Laurikainen, E. and Salo, H. 2002, MNRAS, 337, 1118
- Laurikainen, E. and Salo, H. and Buta, R. and Knapen, J. H. 2007 MNRAS 381, 401
- Laurikainen, E. and Salo, H. and Buta, R. and Knapen, J. H. 2011 MNRAS 418, 1452
- Laurikainen, E., Salo, H., Athanassoula, E. et al. 2014 MNRAS 444, L80
- Laurikainen E., Salo, H. 2016, in Galactic Bulges (Eds. Laurikainen, E, Peletier, R, Gadotti, D), Astrophysics and Space Science Library, Volume 418. Springer International Publishing Switzerland, 2016, p. 77
- Laurikainen, E. and Salo, H., accepted to AA (arXiv:1609.01936)
- Lelli, F., Fraternali, F., Verheijen, M. 2013, MNRAS, 433, L30
- Lütticke R., Dettmar R.-J., Pohlen M. 2000, AAS, 145, 405
- Minchev, I, and Famaey, B. and Quillen, A. et al. 2012 AA 548, A126
- Munoz-Mateos J-C. et al. 2015, ApJS, 219, 3
- Patsis P.A., Skokos Ch., Athanassoula E., 2002, MNRAS 337, 578
- Pfenniger D., Friedli D. 1991, AA, 252, 75
- Quillen, A. C., Minchev, I., Sharma, S., et al. 2014 MNRAS 437, 1284
- Querejeta, M. and Meidt, S. E. and Schinnerer, E. and Cisternas, M. et al. 2015 ApJS 219, 4
- Raha N., Sellwood J. A., James R. A., Kahn F. D., 1991, Nature 352, 411
- Saha K., Martinez-Valpuesta I., Gerhard O., 2012, MNRAS 421, 333
- Salo, H., Laurikainen, E., Laine, J., Comeron, S. et al. 2015 ApJS 219, 4
- Salo, H., Rautiainen, P., Buta, R., et al. 1999, AJ, 117, 792
- Shen, J., and Sellwood, J. A. 2004 ApJ 604, 614
- Sheth, K, et al. 2010 PASP 122, 1397
- Springel, V, Hernquist, L. 2005 ApJ 622, L9

Table 1. Data for galaxies with barlens and X features used in Fig. 6.

Galaxy	Hubble Type	dV_{cir}/dr km/s/kpc	dV_{cir}/dr normalized	V_{max} km/s	h_r kpc	INC degrees	$\log_{10}(M^*/M_{\odot})$
Galaxies with barlenses							
IC2051	SB(<u>rs</u> ,bl)b	223	4.20	155	2.92	53.2	10.58
NGC0613	SB(<u>rs</u> ,bl,nr)b	312	8.12	211	5.50	38.9	11.09
NGC0936	(L)SB _a (<u>rs</u> ,bl)0 ⁺	340	7.90	188	4.37	42.4	10.93
NGC1015	(R')SB(r,bl)0/a	186	5.81	123	3.87	30.5	10.39
NGC1022	(RL)SAB(<u>rs</u> ,bl,ns) <u>0</u> /a	498	6.05	153	1.86	21.6	10.19
NGC1079	(RL)S(<u>A</u> B _a (rs,bl)0	227	4.52	145	2.88	52.4	10.58
NGC1097	(R')SB(rs,bl,nr)ab pec	321	9.63	265	7.96	48.1	11.24
NGC1300	(R')SB(s,bl,nrl)b	227	10.12	122	5.45	33.4	10.58
NGC1302	(RLRL)SAB(<u>rl</u> ,bl)0 ⁺	345	8.77	153	3.89	15.7	10.56
NGC1326	(R ₁)SAB _a (r,bl,nr)0 ⁺	488	7.92	190	3.09	37.2	10.55
NGC1350	(R)SAB _a (r,bl)0/a	273	8.95	158	5.18	58.2	10.82
NGC1398	(R'R)SB(<u>rs</u> ,bl)a	367	9.19	222	5.57	42.2	11.13
NGC1452	(RL)SB(<u>rs</u> ,bl)0/a	242	6.17	133	3.38	53.3	10.40
NGC1512	(RL)SB(r,bl,nr)a	308	7.37	116	2.79	42.7	10.33
NGC1533	(RL)SB(bl)0 ^o	447	5.97	175	2.34	15.6	10.57
NGC1640	(R')SB _a (r,bl)ab	255	4.14	114	1.85	24.1	10.18
NGC2543	SAB(s,bl)b	183	5.56	119	3.61	59.9	10.42
NGC2787	(L)SB _a (r,bl)0 ^o	529	5.64	148	1.59	56.2	10.23
NGC2859	(R)SAB _a (rl,bl,nl,nb)0 ⁺	365	13.93	215	8.20	37.2	10.88
NGC2968	(L)SB(s,bl)0 ⁺	412	6.49	126	1.99	43.1	10.10
NGC3351	(R')SB(r,bl,nr)a	374	7.57	140	2.85	45.0	10.49
NGC3384	(L)SAB(bl)0 ⁻	328	4.96	156	2.37	60.8	10.49
NGC3489	(R)SAB(r,bl)0 ^o :	676	4.57	146	0.99	60.1	10.14
NGC3941	(R)SB _a (bl)0 ^o	559	4.55	179	1.46	50.8	10.49
NGC3953	SB(r,bl)b	227	5.97	162	4.25	58.4	10.99
NGC3992	SB(rs,bl,nb)ab	187	8.77	173	8.10	55.1	11.10
NGC4245	(RL)SB(r,bl,nrl)0 ⁺	423	5.05	95	1.13	33.3	9.80
NGC4314	(R ₁ ')SB(rl,bl,nr)a	414	7.71	118	2.20	20.4	10.14
NGC4371	(L)SB _a (r,bl,nr)0 ⁺	291	7.03	145	3.52	59.0	10.51
NGC4394	(RL)SB(rs,bl,nl)0/a	311	7.95	116	2.97	30.4	10.44
NGC4448	(R)SB(r,bl)0/ <u>a</u>	153	3.75	162	3.95	71.2	10.85
NGC4454	(RL)SAB(r,bl)0/a	182	4.33	143	3.39	17.6	10.66
NGC4548	SB(rs,bl) <u>a</u> b	339	10.55	141	4.39	39.0	10.70
NGC4579	(RLR')SB(rs,bl)a	444	9.04	211	4.30	41.6	11.10
NGC4593	(R')SB(rs,bl,AGN)a	373	11.22	212	6.38	33.4	10.93
NGC4596	(L)SB(rs,bl) <u>0</u> /a	356	8.59	159	3.84	35.5	10.68
NGC4639	(R')SAB(rs,bl)ab	289	4.09	134	1.90	49.2	10.32

Table 1 continued

Table 1 (*continued*)

Galaxy	Hubble Type	dV_{cir}/dr km/s/kpc	dV_{cir}/dr normalized	V_{max} km/s	h_r kpc	INC degrees	$\log_{10}(M^*/M_{\odot})$
NGC4643	(L)SB(<u>rs</u> ,bl,nl)0 ⁺	332	7.45	228	5.11	36.8	11.03
NGC4754	(L)SB _a (bl)0 ^o	393	8.08	167	3.43	59.7	10.64
NGC4795	(R')SAB _a (l,bl)a pec	200	5.05	157	3.98	43.7	10.74
NGC4984	(R'R)SAB _a (l,bl,nl)0/a	479	11.31	217	5.14	53.9	10.69
NGC5101	(R ₁ R ₂ ')SB(<u>rs</u> ,bl)0/a	314	10.07	218	6.99	22.0	11.11
NGC5134	(R)SAB(rs,bl)a	411	4.87	103	1.23	14.7	9.90
NGC5339	SAB(<u>rs</u> ,bl)ab	120	3.84	123	3.94	38.8	10.51
NGC5347	SB(rs,bl)a	427	4.92	174	2.01	22.8	9.90
NGC5375	(R')SB _a (rs,bl) <u>ab</u>	163	6.52	138	5.54	29.8	10.72
NGC5701	(R ₁ ')SAB(<u>rl</u> ,bl)0/a	249	6.92	162	4.51	15.2	10.69
NGC5728	(R ₁)SB(<u>r</u> 'l,bl,nr,nb)0/a	253	8.47	179	6.01	43.0	10.85
NGC5750	(RL)SAB(r' <u>lr</u> ,s,bl)0/a	149	3.79	153	3.90	60.2	10.74
NGC5770	SAB(<u>rl</u> ,bl)0 ⁺	345	4.03	132	1.55	22.4	10.10
NGC5850	(R')SB(r,bl,nr,nb) <u>ab</u>	260	10.46	139	5.59	36.0	10.77
NGC5957	(R')SAB(rs,bl) <u>ab</u>	150	5.88	111	4.37	25.4	10.26
NGC6014	SAB(rs,bl) <u>0</u> /a	191	3.92	119	2.45	35.3	10.33
NGC7079	(L)SAB _a (s,bl)0 ^o :	253	3.64	165	2.38	51.3	10.64
Galaxies with X							
ESO404-027	SAB(s) <u>ab</u> :	71	3.14	78	3.43	69.0	10.13
IC1067	SB(r,bl)b	175	3.34	91	1.74	38.3	9.91
IC3806	SA(r)0 ⁺	62	1.71	65	1.78	65.2	9.49
IC4237	SB(r)b	87	2.21	135	3.41	46.2	10.53
IC5240	SB _x (r)0/a	170	4.80	122	3.44	45.0	10.45
NGC0532	SAB _{xa} (r)0/a	109	3.70	118	4.01	73.6	10.55
NGC0615	(R')SA _x (r) <u>ab</u>	236	4.82	149	3.05	66.0	10.54
NGC0779	(L)SA _x (rs)a	175	2.50	130	1.86	70.3	10.35
NGC1461	SAB(r)0 ^o	231	3.90	131	2.21	70.8	10.40
NGC1476	Im sp	40	1.36	44	1.48	66.3	9.14
NGC2654	SB _x (r,nd)0/a sp	175	2.81	146	2.35	74.3	10.56
NGC2683	(R'L)SB _{xa} (rs)0/a sp	236	3.30	163	2.29	74.9	10.62
NGC3185	(RL)SAB _{ax} (rs,bl)a	237	4.59	115	2.23	49.5	10.22
NGC3254	SAB _{xa} b	111	5.64	106	5.40	73.3	10.57
NGC3301	(R'L)SAB _x (r)0 ⁺ sp	286	6.13	139	2.99	71.7	10.45
NGC3380	(RL)SAB(<u>rs</u> ,bl)0/a	204	3.98	102	1.99	20.8	9.96
NGC3424	S _x <u>ab</u> : sp pec	173	3.42	143	2.83	75.8	10.43
NGC3623	(R')SAB _x (rs)a	231	5.25	175	3.98	73.7	10.91
NGC3673	(R')SAB _x (rs)ab	166	4.65	122	3.41	52.6	10.51
NGC3692	(R'L)SA(r)0/a sp	94	1.76	135	2.51	75.6	10.54
NGC3887	(RL)SAB _x (rs)bc	193	3.38	145	2.54	32.9	10.48
NGC4123	SB _x (rs) <u>ab</u>	259	10.42*	99	3.99	46.9	10.29

Table 1 continued

Table 1 (*continued*)

Galaxy	Hubble Type	dV_{cir}/dr km/s/kpc	dV_{cir}/dr normalized	V_{max} km/s	h_r kpc	INC degrees	$\log_{10}(M^*/M_{\odot})$
NGC4192	(R ₁ ')SAB _x (rs,nd) <u>a</u> b	270	13.06	140	6.79	72.0	10.77
NGC4216	(R ₂ ')SAB _{ax} (r,nd) <u>a</u> b sp/E7-8	194	6.76	158	5.50	79.6	11.00
NGC4220	(L)SAB(r)0 ⁺	189	2.61	130	1.79	72.4	10.36
NGC4235	S _x 0 ⁺ sp	257	5.28	135	2.77	72.0	10.50
NGC4268	SAB(<u>rs</u>)0 ⁺ : sp	194	3.80	121	2.38	60.9	10.24
NGC4293	R(L)SB _x (<u>rs</u>)0/a	313	9.15	119	3.48	62.1	10.42
NGC4419	SAB _x 0/ <u>a</u> sp/E6	331	2.96	165	1.48	71.3	10.46
NGC4462	SAB _x (rs)a	188	3.70	137	2.69	63.3	10.54
NGC4569	(R'L)SAB _x (rs,x ₁ r)a	391	11.32	136	3.96	66.0	10.64
NGC4586	SAB _x (s,nd)0/a sp	218	6.32	90	2.62	69.8	10.13
NGC4725	(R')SAB _x (r,nb)a	366	10.90*	162	4.84	46.8	10.88
NGC4818	(RL)SAB _{xa} (s)0o	342	7.52	141	3.10	67.2	10.48
NGC4845	(R'L)SAB _x (r'l,nd)0/a	262	10.59	135	5.44	75.1	10.55
NGC4856	(RL)SB0 ⁻	277	5.75	172	3.58	68.7	10.74
NGC4902	SB(<u>rs</u> ,bl) <u>a</u> b	206	4.23	209	4.30	21.5	11.05
NGC5005	(R ₂ ')SAB _{xa} (rs)ab	396	5.99	244	3.70	66.7	11.10
NGC5297	SAB _x (s)bc sp	78	2.57	126	4.16	73.6	10.60
NGC5443	(R'L)SAB _x (rs)a sp	139	5.08	119	4.36	68.0	10.49
NGC5448	(R ₁ L)SAB _x (<u>rs</u>)a	167	8.43	143	7.24	65.4	10.77
NGC5689	(R'L)SAB _x (r'l,nd)0/a	181	5.85	171	5.53	74.4	10.84
NGC5757	(R')SB(rs) <u>a</u> b	248	4.65	177	3.32	32.7	10.74
NGC5806	(R'L)SAB(rs,nrl)ab	228	4.20	147	2.72	56.5	10.59
NGC5854	(RL)SAB _x (rl)0 ⁺ sp	189	3.76	119	2.37	71.1	10.23
NGC5864	(RL)SB _{xa} 0 ⁺ sp	139	2.48	120	2.14	71.6	10.35
NGC5878	SAB _{xa} (rs)ab	185	5.13	149	4.14	68.1	10.77
NGC7140	(R')SAB _x (rs,nrl) <u>a</u> b	161	7.39*	126	5.80	49.8	10.70
NGC7163	SAB _x (s)a	206	5.46	101	2.67	57.5	10.13
NGC7171	SAB _x (s)b	87	2.82	127	4.13	57.5	10.58
NGC7179	SB _{xa} (<u>r'l</u>)0/a	100	2.48	135	3.33	58.9	10.60
NGC7421	(R')SB(rs,bl)ab	132	2.93	102	2.26	27.9	10.15
NGC7513	(R'L)SB(rs)a	102	3.09	101	3.05	48.4	10.21
NGC7531	SAB _x (r)a	221	3.90	144	2.55	57.5	10.44
PGC045650	SAB _a (s)ab	185	2.38	136	1.76	72.7	10.37

NOTE—The inner slope dV_{cir}/dr and the maximum velocity V_{max} are calculated from the S⁴G 3.6 μ m images, the stellar masses M^* are from (Munoz-Mateos et al. 2015), the disk scale length and inclination are from Salo et al. (2015). Normalized dV_{cir}/dr indicates scaling of the inner slope with V_{max}/h_r : the X-shape galaxies with $i < 60^\circ$ and normalized $dV_{cir}/dr > 8$ are marked with an asterisk. The barlens classifications are from Buta et al. (2015) and Laurikainen et al. (2011), and the X classifications from Laurikainen & Salo (2016).